Fundamentals of 3-D Neutron Kinetics and Current Status

José M. Aragonés

Departamento de Ingeniería Nuclear, Universidad Politécnica de Madrid, 28006 Madrid, España

Abstract. This lecture includes the following topics: 1) A summary of the cell and lattice calculations used to generate the neutron reaction data for neutron kinetics, including the spectral and burnup calculations of LWR cells and fuel assembly lattices, and the main nodal kinetics parameters: mean neutron generation time and delayed neutron fraction; 2) the features of the advanced nodal methods for 3-D LWR core physics, including the treatment of partially inserted control rods, fuel assembly grids, fuel burnup and xenon and samarium transients, and excore detector responses, that are essential for core surveillance, axial offset control and operating transient analysis; 3) the advanced nodal methods for 3-D LWR core neutron kinetics (best estimate safety analysis, real-time simulation); and 4) example applications to 3-D neutron kinetics problems in transient analysis of PWR cores, including model, benchmark and operational transients without, or with simple, thermal-hydraulics feedback.

1. CELL AND LATTICE CALCULATIONS TO GENERATE NEUTRON KINETICS DATA

In this lecture we assume that the fundamental theory of neutron kinetics (NK) is known from classical text books [1-5], and we will address the more advanced issues that are relevant for 3-D NK [6-32]. The first and preliminary issue is the generation of the neutron reaction data to properly model in 3-D the large operating light water reactors with the state-of-the-art nodal codes. It requires the use of advanced cell and lattice codes and elaborated methods [33-38] for the homogenization of the increasingly heterogeneous fuel assemblies, due to the introduction of advanced fuel and burnable absorber design options.

The cell and assembly averaged two-group cross sections and discontinuity factors are calculated by a complete and consistent set of fuel assembly calculations in the full parameter space, including nominal burnup, branch, off-nominal burnup and neighborhood cases [21-22, 26-27, 30-31]. The 2-group cell or node homogenized cross sections, and transport-equivalent discontinuity factors [10-11, 13], are fitted by multivariable least-squares techniques, including the partial derivatives with each state variable: water density and temperature, fuel temperature, boron, and xenon plus samarium absorptions.

The additional "generalized state" variables required for advanced nodal calculations are: the spectral history index (equivalence of the different burnup paths in parameter space) and the boundary indexes, to account for the intragroup spectral effects due to changes in the boundary conditions by the different kinds of neighbor cells or nodes. For neutron kinetics calculations the main nodal kinetics parameters that are also required for every fuel assembly type are: the mean neutron generation time and the effective delayed neutron fraction.

1.1. Spectral History and Neighborhood Effects

The spectral history effect is due to the differences in the destruction and buildup rates of the fuel nuclides, specially ^{235}U and ^{239}Pu in UO_2 fuels, that change both with the spectrum and with the effective cross sections by Doppler and self-shielding effects [8] and, thus, with the burnup history path in state-conditions space. In few-group microscopic burnup calculations, the problem is reduced to the proper treatment of the broadening, shielding and averaging of the microscopic cross sections, and to the consistent flux solution; but this approach is impractical for whole core problems. In practical 2-group macroscopic burnup calculations, the differences in fuel nuclides composition due to the burnup history should be accounted for in all the macroscopic cross sections.

The spectral history effect for a typical PWR fuel assembly, 17x17 all Zircaloy with 3.60 w/o enrichment, is summarized in figure 1. Its shows the reactivity deviation, or error in K-infinity without spectral history treatment, as a function of fuel burnup for several off-nominal history conditions of the relevant state variables: water density, fuel

temperature and Boron concentration. These off-nominal conditions bound the operational range of variation in PWR cores around the average nominal values (0.70 g.cm^{-3} water density, 100 % power and 750 ppm Boron).

Previous approaches have approximated the history effect in terms of simple spectral indexes averaged along burnup, including the fast-to-thermal flux ratio, and the fast-to-total fissions or burnup ratio. We have found that, when applied to all the Σ's, the last index improves the joint correlation of the off-nominal water density and Boron histories, as is shown in figure 2 (left); but both fail to reduce the error of the off-nominal power or fuel temperature histories, from the uncorrected deviations of 500 to 600 pcm (fig. 1), to about ±400 pcm at 40 MWd/kg.

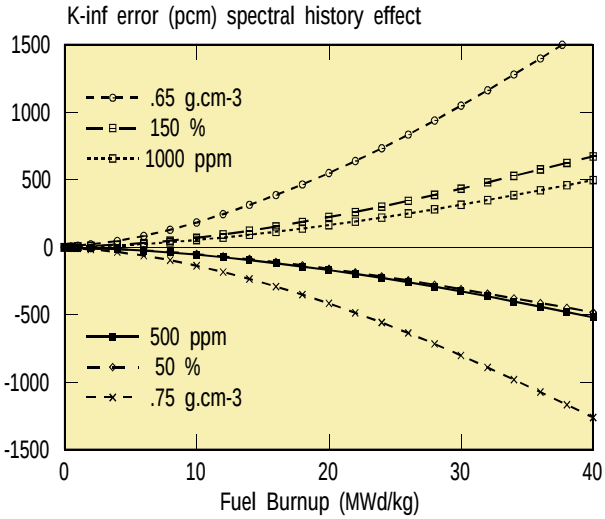

Figure 1. Deviation of the fuel element reactivity along burnup at several off-nominal history conditions of water density, fuel temperature and Boron; without spectral history treatment.

We found that the changes in fuel temperature modify directly the ^{239}Pu production rate, and hence the reactivity, but change very little those previous spectral indexes. To account this effect, we have introduced [21-22, 27] the normalized resonance absorption probability multiplied by the ratio of fast absorptions to total fissions, resulting in the following generalized spectral history index:

$$SH = \frac{\Sigma_{a1}}{\Sigma_{a1} + \Sigma^{*}_{1\to 2}} \cdot \frac{\Sigma_{a1}\phi_1}{\Sigma_{f1}\phi_1 + \Sigma_{f2}\phi_2} \qquad (1)$$

in terms of the macroscopic absorption, fission and downscatter ($\Sigma^{*}_{1\to 2}$) cross sections and the two-group fluxes.

The results obtained with this generalized spectral history index are shown in figure 2 (right), for the same PWR fuel assembly and off-nominal histories of figure 1. Note that the whole scale of errors is reduced by more than one order of magnitude, bringing down the errors of the off-nominal burnup cases to the ±20 pcm level, similar to the linear fits of the branch cases at every burnup. The advantage of including all the history effects through a single generalized index is not only the saving in storage, but the confidence in really equivalencing every history path in the multivariable operating space.

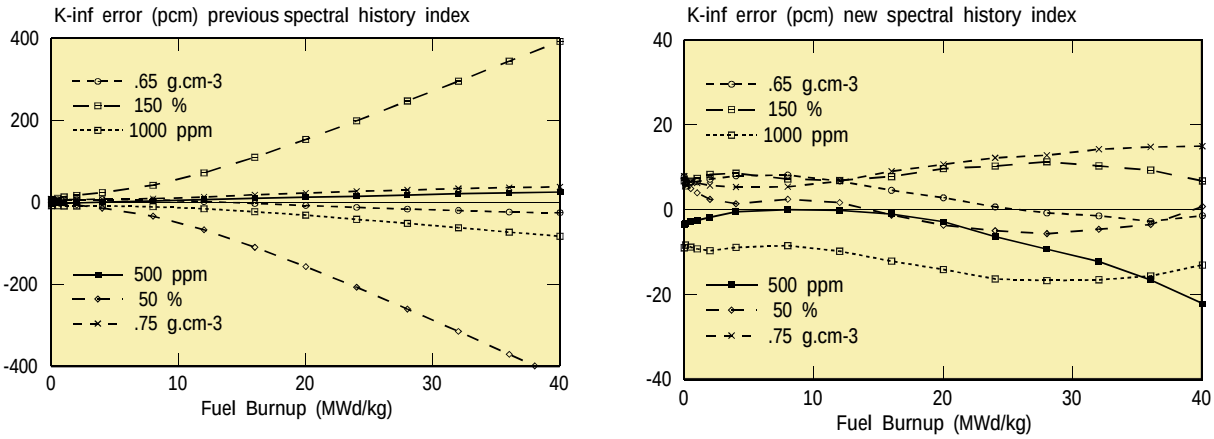

Figure 2. Errors of assembly reactivity along burnup at several off-nominal conditions of water density, fuel temperature and Boron. Previous (left) and new (right) spectral history index.

The new treatment of the intragroup spectral change in each cell type, due to the actual boundary currents with different neighbor cells, includes the various configurations of fuel rods with water guide-tubes, control rods and burnable absorber tubes or gadolinium fuel rods in any location within the assembly. The changes in the 2-group cross sections and discontinuity factors, in relation to the regular or reference pin-cells, are related and fitted to the

local and global leakages (or bucklings) per group.

The libraries per cell type are used [21-22, 27] in our COBAYA extended code to interpolate, cell-by-cell at the actual local conditions and locations, the 2-group cross sections and the discontinuity factors used in the 2-D fine-mesh diffusion calculations of the actual core configuration at selected core planes, covering the range of operating conditions along the cycle. COBAYA performs the homogenization over the quarter-of-assembly nodes of the 2-group cross sections and discontinuity factors per nodal interface, including the reflector, using the intranodal heterogeneous flux solutions for the whole core planes.

These nodal 2-group constants, to be used by SIMTRAN, are parameterized per node type in the same way as the cell library, including all the partial derivatives with state variables and the new spectral history and neighborhood indexes [27, 32-33]. Both the cross sections and the discontinuity factors account for changes in the boundary conditions at each nodal interface, due to control or burnable absorber rods, gadolinium pins and actual burnup gradients within the node and its neighbors. In the nodal constants we also include the ratios of the peak pin powers, and fission rates at the incore detectors, to the interpolated intranodal power. With this extended synthetic parameterization of the nodal constants, the 3-D nodal solution and the pin power reconstruction in SIMTRAN are fast and accurate [33].

1.2. Nodal Kinetics Parameters: Mean Neutron Generation Time and Delayed Neutron Fraction

The mean neutron generation time is calculated for every fuel assembly type in the lattice code by a weighting in energy and space with the neutron flux of the inverse neutron speed, divided by the integral of the fission source:

$$\Lambda = \frac{\int_V \int_0^\infty \frac{1}{v(E)} \phi(r,E)\, dE\, dr}{\int_V \int_0^\infty F\, \phi(r,E)\, dE\, dr} \quad ; \quad \Lambda = f\,(\,Burnup, Boron\,, Xe\,, T_{eff}\,, \rho_{\mathrm{mod}}\,) \tag{2}$$

The effective delayed neutron fraction is also calculated for every fuel assembly type in the lattice code by a weighting in energy and space of the delayed neutron source, divided by the integral total fission source:

$$\beta = \frac{\sum_i \sum_k \int_V \int_0^\infty [\ \chi_{d\,k\,i}(E) \int_0^\infty \nu_{dki}\, \Sigma_{f\,i}(r,E')\, \phi(r,E')\, d'E\ ]\, dE\, dr}{\int_V \int_0^\infty F\, \phi(r,E)\, dE\, dr} \quad ; \quad \beta = f\,(\,Burnup) \tag{3}$$

In figure 3, we plot these parameters for a typical PWR fuel assembly as a function of the burnup. The mean neutron generation time changes quite closely to the Boron worth, since the last has a ***1/v*** cross section. The effective delayed neutron fraction decreases with burnup, since the Plutonium isotopes produce less delayed neutrons than the Uranium.

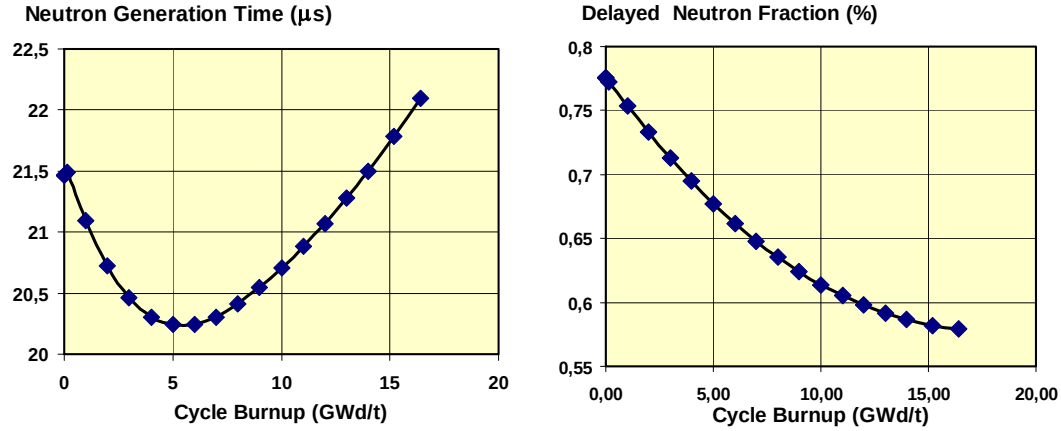

Figure 3. Evolution with burnup of the mean neutron generation time (left) and the effective delayed neutron fraction (right) for a typical PWR fuel assembly.

2. ADVANCED NODAL METHODS FOR 3-D CORE PHYSICS

2.1. Improved Internal Core 3-D Calculation

Axial nodal effects and explicit grid modeling have been improved in SIMTRAN, by using a variable and adapted axial mesh, in 34 nodes, so that the grids are centered in the corresponding nodes and a finer mesh is used near the fuel extremes. The grids are explicitly modeled in reference 3-D 2-group SIMTRAN calculations, with embedded finer mesh axial solutions [19], that provide the grid homogenization and the synthesis of axial discontinuity factors and albedos. The control rod "cusping" effect has also been solved, to smooth out the differential worth at intranodal insertions.

The 3-D transient treatment of fission products has been improved and extended [16, 21]. The nodal concentrations of ^{135}I, ^{135}Xe, ^{149}Pm and ^{149}Sm are updated explicitly at every time step, including decay and locally dependent fission yields and absorption rates. Following the conclusions of our previous study [16], including all the fission products with significant transient behavior, we reduce the ^{149}Pm $\rightarrow$ ^{149}Sm chain to its production via ^{149}Nd, because in the via ^{147}Nd $\rightarrow$ ^{147}Pm $\rightarrow$ ^{148}Pm + ^{148m}Pm $\rightarrow$ ^{149}Pm, the increase in ^{149}Sm absorptions by decay of the extra ^{149}Pm is rather closely compensated by the decrease in ^{148}Pm and ^{148m}Pm absorptions, although with different decay periods.

This is shown in figure 4, which plots the decrease in reactivity that results from the net change in absorptions by decay of those nuclides as a function of the time after shutdown, from several power levels at 30 MWd/kg of burnup for typical PWR fuel.

Note that in this calculation only the via from ^{147}Nd is considered. We conclude that the net transient effect of this via is rather small and shifts in sign for long shutdowns. For lower burnup the slow accumulation of ^{147}Pm reduces even more the amplitude of the oscillation, while it saturates for higher burnup.

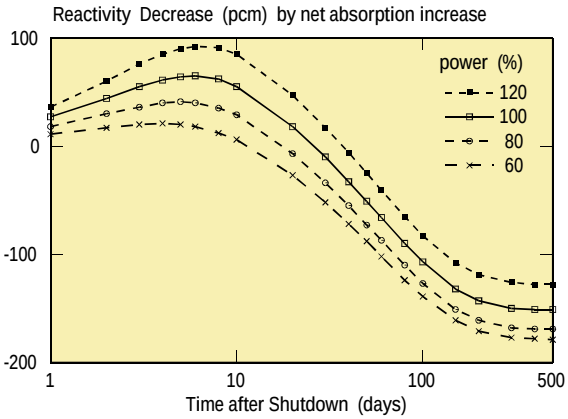

Figure 4. Reactivity decrease (pcm) by net absorption due to decay of extra ^{149}Pm (only via ^{147}Pm), ^{148}Pm and ^{148m}Pm after shutdown from several power levels.

The calculation of the isotopic depletion in ^{10}B of the soluble Boron in the primary system, by neutron absorption during the residence of the borated water in the core, has also been implemented in SIMTRAN, following our previously published method [17]. In the online version the actual borations -with new boric acid of natural abundance- are taken into account to compute the actual isotopic abundance in the primary along cycle burnup.

2.2. Excore Detector Response Calculation

The detector responses at the 8 excore chambers of the power range, in terms of currents proportional to the BF_3 reaction rates for thermal neutrons, are basically proportional to the fast neutron flux that passing through the radial water reflector, internal structures and reactor vessel reaches the well cavity, where it is reflected and moderated at the concrete walls and at the polyethylene envelopes of the detectors, if present. The effect of the change in fast flux attenuation with the density of the water reflectors, it is with the inlet cold-leg temperature, should be properly accounted for.

A detailed online method, to solve the 3-D multigroup neutron transport problem, was excluded due to computing time limitations and uncertainties in the actual configuration of the reactor internals, external thermal insulation and piping, and excore wells. We adopted [20-21] a response matrix approach to calculate the reaction rates integrated over each excore detector, in terms of the neutron leakage across every fuel node face in the core-reflector boundary viewed from each excore detector, located in the diagonals of each quadrant. The reaction rate at the excore chamber ***c*** is given by:

$$R_c = \sum_{n=1}^{next} \sum_{k=1}^{kmax} A_{n,k \Rightarrow c} \; J_{n,k} \tag{4}$$

The currents $\boldsymbol{J_{n,k}}$ through the core-reflector interface of external node ***n***, at the elevation ***k***, are directly available from the 3-D nodal core solution, including the incore flux redistributions with the core (and reflector) conditions.

The excore response matrix $A_{n,k \Rightarrow c}$ is the probability for neutrons leaking through face ***n,k*** to yield a response in detector ***c***, and is unique to a good approximation, as far as the vessel internals and external cavity and detector configurations are not significantly modified during the plant lifetime, except for the spectral variation of the core neutron leakage with incore water density, which has been found negligible, and for the already mentioned effect of change of the reflector attenuation with the inlet water density, where the Boron effect is also negligible.

$$A_{n,k \Rightarrow c} = \frac{next \,.\, kmax}{\sum_{n=1}^{next} \sum_{k=1}^{kmax} A_{n,k \Rightarrow c}} \sum_{k_c=1}^{nk_c} \sum_{\forall p \in n,k \Rightarrow k_c} \exp\left(- \sum_{r \in p} x_{p \Rightarrow r} \Sigma_r^{*} \right) \tag{5}$$

The response matrix has been calculated as function of the effective average optical thickness through the water and steel regions ***r***, computed by a ray-tracing technique, that traces in 3-D a set of paths ***p*** from the center of each node face ***n,k*** in the core periphery to each axial section k_c of the excore detector ***c***, computing the thickness $x_{p \Rightarrow r}$ of the intersections of each path with every region, as sketched in figures 5, left and right, but including the 3-D paths reflected at the cavity wall (hence the use of $\Rightarrow$).

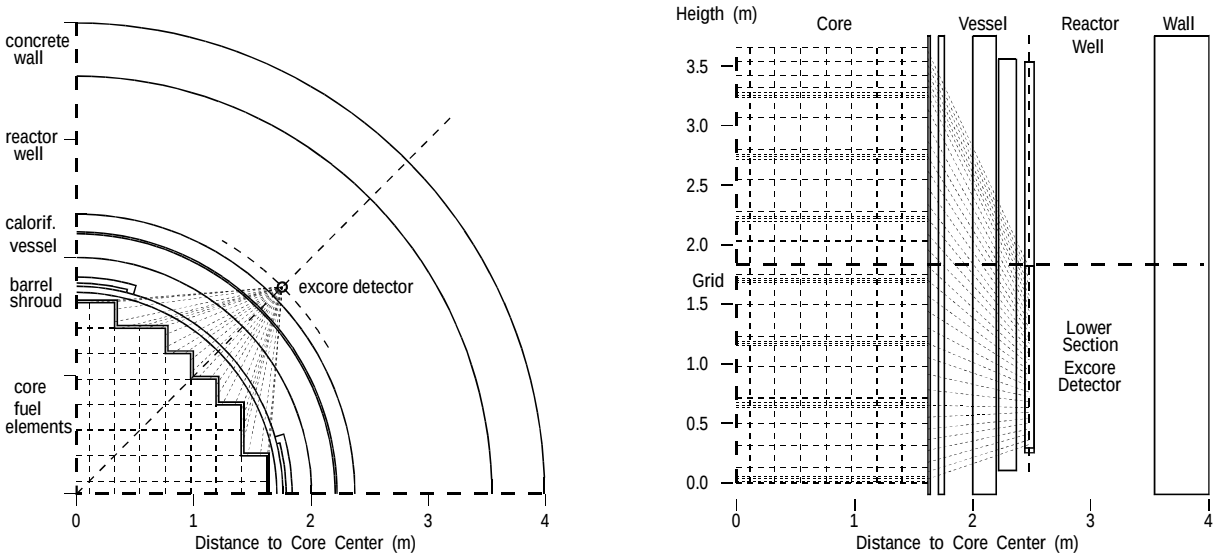

Figure 5. Horizontal (left) and vertical (right) sections of core (with fuel elements, nodes and grids), shroud, barrel, vessel, calorifuge, excore detector (lower section), reactor well and wall. Only the direct lines-of-sight from core-boundary to detector are shown.

The effective attenuation cross sections Σ_r^{*} for each water reflector, steel and cavity well region were precalculated by a 24-group S_6 discrete ordinates solution of the whole core, reflector with water and support plate and internals, vessel and concrete wall in 1-D cylindrical geometry. By perturbing the density of each region, the logarithmic change of the ^{10}B reaction rate in the excore detector location, divided by the region physical thickness, directly provides the effective attenuation. These neutron transport calculations show that the reflections at the cavity wall increase the ^{10}B reaction rates by several orders of magnitude and flatten the fast and thermal fluxes inside the cavity.

The exponential variation with the effective water optical thickness, proportional to its density, of each response matrix element has been linearized around the nominal inlet water density, introducing an additional matrix $W_{n,k \Rightarrow c}$, the water optical thickness averaged over the set of paths from the node faces ***n,k*** to detector ***c***, that accounts for the reflector water density variation, by:

$$A_{n,k \Rightarrow c} = A_{n,k \Rightarrow c}(\rho_0) \left[1 + W_{n,k \Rightarrow c} \left(1 - \frac{\rho}{\rho_0} \right) \right] \tag{6}$$

Since the actual detector efficiencies are unknown, and the gains in the instrumentation chains are adjusted during calibration tests, the response matrix is normalized to unity average response per nodal face, and the actual response-to-current factors should be calibrated to the measured values for each detector.

This excore response matrix method has been validated [20-21] with the actual excore currents registered during

the test to measure the moderator temperature coefficient (MTC) at power, near 300 ppm at the end of cycle 6 in the Vandellòs-II PWR. This test was replicated with SIMTRAN following the measured evolution, at 10 minutes time steps, of the inlet water temperature, that drops about 2.5 ºC in 1.5 hours, stabilizes during 1 hour and rises back in about 2 hours. The core thermal power, water flow and control rod insertion are kept almost constant. The xenon is redistributed, with all other nodal variables, along the 3-D simulation. The predicted critical boron concentration follows closely the measured boration/dilution of about 15 ppm, so that the MTC is well predicted.

Since the simulation is 1/8 core symmetric, only the relative change in the sum of the currents of the 8 excore detectors (sum-I) and the relative axial difference of the currents (delta-I), in the top minus the bottom detectors are relevant. The results of the calculated evolution of sum-I and delta-I are plotted in figure 6, together with the measured ones.

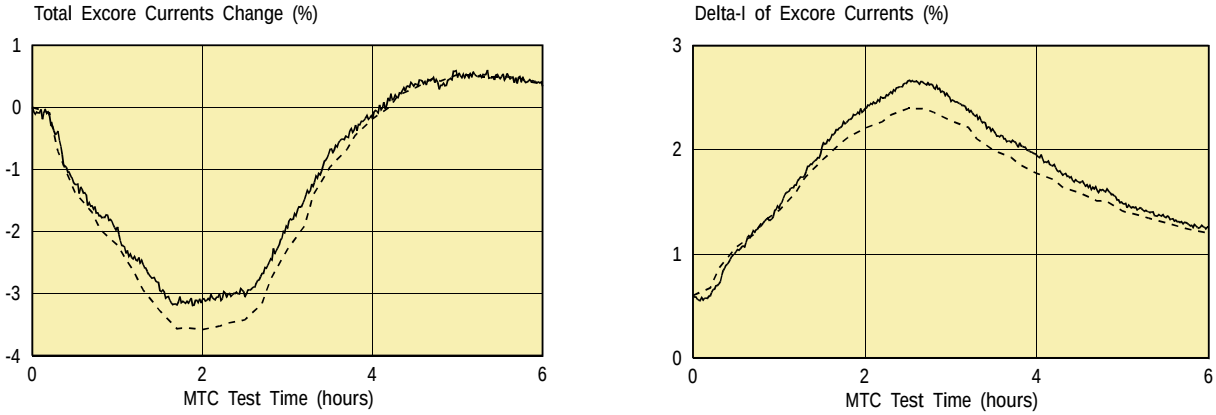

Figure 6. Relative change (%) of the total excore currents (sum-I, left) and axial difference (delta-I, right), as measured (solid) and calculated by SIMTRAN (dashed).

The SIMTRAN results follow very closely the decrease of about 3 % in the total excore response, with a slight overprediction, and the increase of about 2.5 % in the axial current difference, with a small underprediction. Note that following these results; inlet temperature asymmetries per loop of 1 ºC can induce asymmetries in the excore currents per quadrant of about 1 %, and similar changes in the axial differences of excore currents.

Figure 7 (left) plots the results of the incore-excore cross calibrations as performed with the measured and online calculated data. The points used for the linear fits were obtained from the full (4) and partial (4) incore flux maps actually measured during the axial oscillation at 75 % power and the first map at full power, near equilibrium Xenon, with the corresponding registers of the excore currents and the SIMTRAN online calculations at the same times. A one-point calibration of the calculated axial offset of incore power was done at the full power point. The differences between the linear fits to measures and calculations are below ±1 % at the extremes of the calibration range (-8 % to +7 % in incore A.O.) that is within the quality acceptance criterion of ±3 %.

Figure 7 (right) plots the results of the calibration for the excore currents at the upper and lower sections of excore N-42 as a function of the incore A.O., using the corresponding measured and calculated points at the same flux maps taken at 75% power. Both fits are also in very good agreement, with similar deviation in the points at the full power map.

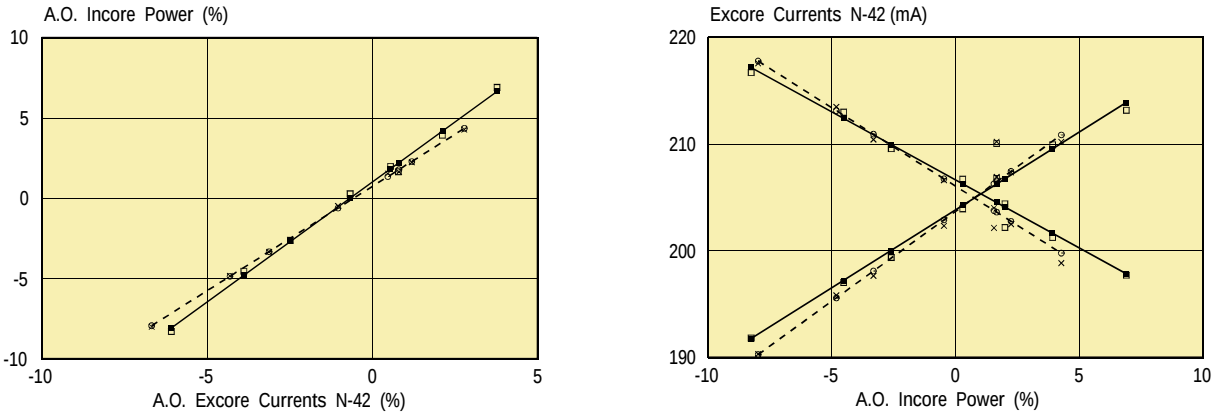

Figure 7. Incore-excore calibration (left) and excore currents (right) at upper and lower sections of detector N-42: measurements and linear fit (solid) and Simtran predictions (dashed).

Finally, figure 8 (left) shows the measured and calculated paths in the power versus incore delta-I surveillance plot, as registered every 5 minutes along 32 hours, during a routine operating procedure at partial power, for valves testing, in cycle 8 (12-13 august 1995). In this maneuver, power was reduced from 100 to 72 % in 9 hours, kept at the 72-76 % level during 4.5 hours, and brought back to ≈100 % in 4 hours. The measured incore delta-I was obtained by the process computer, using the previous incore-excore calibration from the excore axial differences of currents, while SIMTRAN provides directly the axial relative difference of the incore power distribution. Figure 8 (right), shows the same plot for an actual maneuver of return to power after a short shutdown. The C-M differences are within ±0.5 %, within the allowed delta-I bandwidth of ±5 % shown in background of this plot as a sketch of the constant axial offset control (CAOC) technical specification.

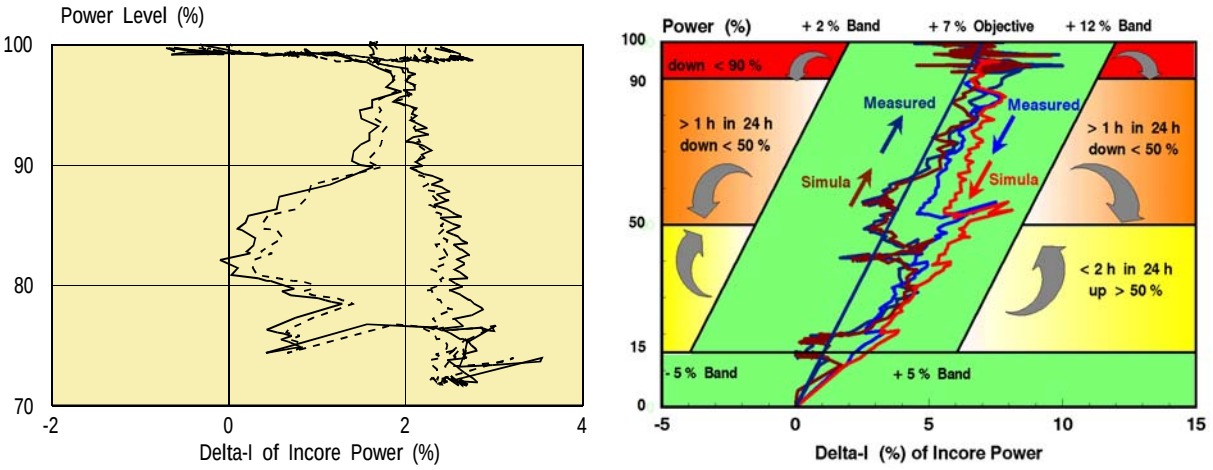

Figure 8. At left, surveillance (left) of the axial power difference during an actual operational maneuver of load reduction, including the measurements (dashed) and Simtran (solid). At right, measured (blue) and simulated by Simtran (red) power vs. axial asymmetry of power in a return to power actual maneuver after a short shutdown.

3. ADVANCED NODAL METHODS FOR 3-D CORE NEUTRON KINETICS

3.1. The equations of 3-D neutron kinetics

We will consider the one-group time-dependent neutron diffusion equations, to focus on the time dependence and its discretization, since the extension to multigroups is straightforward. The equation of the 3-D nodal neutron kinetics is coupled to the evolution equations of the families or groups (normally 6) of precursors of delayed neutrons:

$$\Lambda_l \frac{dS_l}{dt} = \sum_{m=1}^{6} (W_{ml} S_m - W_{lm} S_l) - \frac{S_l}{k_{\infty l}} + (1 - \beta_l) S_l + \sum_{k=1}^{6} \lambda_k C_{kl}$$
$$\frac{dC_{kl}}{dt} = f_k \beta_l S_l - \lambda_k C_{kl} \quad ; \quad k = 1,\ldots,6 \tag{7}$$

Where the new parameters are:

- Λ_l mean neutron generation time in node *l*.
- β_l effective delayed neutron fraction in node *l*.
- C_{kl} concentration of the precursor family *k* in node *l*.
- f_k relative distribution of precursor family *k*.
- λ_k decay constant of the precursor family *k*.

The fission sources are separated in that due to the prompt neutrons, a fraction (1-β) of total, and that due to the delayed neutrons, a fraction β of total, that are produced by the decay of the precursor fission products, grouped in six families with different decay constants (λ).

Note that by difference with the static case, this time dependent equation is not any more an eigenvalue problem [7], but an initial value problem, with an "external" source arising from the source of the previous time step and the delayed neutron source, although the last is related with the total neutron source.

3.2. The solution with time of the equations of 3-D neutron kinetics

The fission source (S_l) is discretized by the exponential extrapolation:

$$S_l(t) = s_l(t)\, e^{\omega_l t} \tag{8}$$

Where $s_l(t)$ will be a slowly changing function if the frequencies ω_l are conveniently updated at each time step, so that its the time derivative will be well approximated (implicitly) by the first order difference:

$$\left.\frac{ds_l(t)}{dt}\right]_{t=\Delta t} = \frac{s_l(\Delta t) - s_l^0}{\Delta t} \tag{9}$$

$$\left.\frac{dS_l}{dt}\right]_{t=\Delta t} = \left(\omega_l + \frac{1}{\Delta t} \right) S_l(\Delta t) - \frac{e^{\omega_l \Delta t}}{\Delta t} S_l^0 \tag{10}$$

The time variation of the precursor densities ($C_{kl}(t)$, *k=1, ..., 6*) also is smooth, so that:

$$\frac{dC_{kl}}{dt} = \frac{C_{kl} - C_{kl}^0}{\Delta t} \; ; \; C_{kl} = \frac{f_k \beta_l S_l \Delta t + C_{kl}^0}{1 + \lambda_k \Delta t} \tag{11}$$

3.3. Solution of the 3-D neutron kinetics equations in a nodal code (SIMTRAN)

To solve the NK equations, with six groups of delayed neutron precursors, we use a forward linear time differencing for the six precursor concentration equations, so that they are implicitly substituted in the fission source nodal equations. The exponential expansion in time of the fission source, with nodal frequencies from the previous time step, and its linear time differencing results in the following non-diagonal linear system:

$$\left(\sum_{m=1}^{6} W_{nm} + \frac{1}{k_{\infty n}} - 1 + \frac{\Lambda_n}{\Delta t} + \Lambda_n \omega_n + \beta_n \sum_{d=1}^{6} \frac{f_d}{1 + \lambda_d \Delta t} \right) S_n - \sum_{m=1}^{6} W_{mn} S_m = \frac{\Lambda_n}{\Delta t} S_n^0 e^{\omega_n \Delta t} + \sum_{d=1}^{6} \frac{\lambda_d C_{dn}^0}{1 + \lambda_d \Delta t} \tag{12}$$

Where:

- S_n is the relative fission source of node *n* at time *t*, with superscript 0 at time (*t*-Δt).
- $k_{\infty n}$ is the infinite multiplication factor (fission source over absorptions) of node *n*.
- $W_{n\,m}$ is the finite-difference synthetic coefficient, such that $(W_{n\,m} S_n - W_{m\,n} S_m)$ is the net neutron leakage from node *n* to node *m* (6).
- Λ_n is the mean neutron generation time (s) of node *n*.
- Δt is the time step (s).

ω_n is the exponential frequency (s^{-1}) of the fission source at node n, given by

$$\omega_n = \frac{1}{\Delta t} \ln \frac{S_n(t)}{S_n^0(t-\Delta t)} \tag{13}$$

β_n is the effective fraction of delayed neutrons per fission of node n.
f_d is the fraction of the delayed neutron precursor group d (d=1,6).
λ_d is the half-life (s^{-1}) of the delayed neutron precursor group d.
$C_{d\,n}^0$ is the relative nodal concentration of the delayed neutron precursor group d of node n at the previous time step (t-Δt).

Note that the extra diagonal terms (fourth to sixth in equation 12) are small and positive, except for large negative frequencies (during rod trips), that are moved to the source term in the right-hand-side of the equation. This property preserves the diagonal dominance of the linear system, required for quick convergence of standard iterative methods, such as the tri-diagonal inversion on axial lines of nodes with over-relaxed Gauss-Seidel on the X-Y node lines.

SIMTRAN is our 3-D nodal neutron kinetics (NK) code for PWR cores [19]. It solves the neutron diffusion equations, in 1 or 2 groups, on coarse-mesh nodes (quarters of fuel assemblies) using a linear-discontinuous finite-difference scheme [10-11,13], where the interface net currents are given in terms of the actual node average and the corrected interface averaged fluxes, using interface flux discontinuity factors (IFDFs) for each group and node-interface, that are pre-calculated by 2-D pin-by-pin 2-group diffusion calculations of whole core planes.

The coefficients of the one-group equation (12) are iteratively calculated from the embedded two-group 1-D axial fine-mesh diffusion solutions for each node stack. The full two-group 3-D nodal neutron flux solution is directly obtained from the nodal fission sources and the converged fast-to-thermal flux ratios of the 1-D axial solutions. Only a few (<5) outer and (<20) inner iterations are required for convergence at every time step, using an exponential extrapolation of the nodal sources and fluxes to advance the time step and a harmonic interpolation from the axial nodal mesh to the fine-mesh (4 or 8 fine intervals per node, with 34 nodes in the active core).

4. EXAMPLE APPLICATIONS: 3-D NEUTRON KINETICS PROBLEMS IN PWR CORES

4.1. Analysis of the Dynamic Rod Worth Measurement at cycle startup tests

Using our SIMTRAN code, we have done a detailed analysis by static and dynamic calculations, of the test for Dynamic Rod Worth Measurement (DRWM), that is performed during the physical tests at beginning of the cycles in the Spanish Nuclear Power Plants with Westinghouse-PWRs [19].

With the static and dynamic factors obtained by SIMTRAN we have analyzed the actual test results, from the measured excore currents, obtaining an excellent agreement with the results of the Plant Reactivity Computer, determined with the factors supplied by Westinghouse [19].

4.1.1. Static Calculations of Control Bank Worth and Static Spatial Factors

The static calculations of the control bank worth, at beginning-of-cycle (BOC) and hot-zero-power (HZP), are done with a reduced version of the SIMTRAN code, without 3-D kinetics or thermal-hydraulic feedback. As a routine, the SIMTRAN databases for each cycle include the response matrices of the 8 excore detectors to the neutron leakage at the core boundary (see §1.2). In figure 9 (left) we plot the integral control bank worth for each bank, as a function of its insertion (full-in at 0 steps, left, full-out at 225 steps, right), calculated at BOC-HZP of cycle 14 of the Ascó-II plant.

As any control bank is inserted, it causes the neutron flux redistribution within the core, both radially and, even more, axially. Hence, to obtain the level of the total, or average, neutron flux or power in the core from the measured currents in the excore detectors, we have to deal with these spatial redistribution effects in the core and, through the changes in the neutron core leakage, in the response of the excore detectors. To that purpose, Chao et al. [19] have introduced the "Static Spatial Factors" (SSF), for the superior and inferior detectors of the excore channel (N-44) used in the measurement. The SSF are defined, in function of the bank insertion, as the ratio between the current calculated in each detector at such insertion and the current calculated with all rods out (ARO).

Figure 9 (right) plots the calculated SSF for both excore detectors, superior and inferior, as a function of the bank insertion, from the SIMTRAN excore currents.

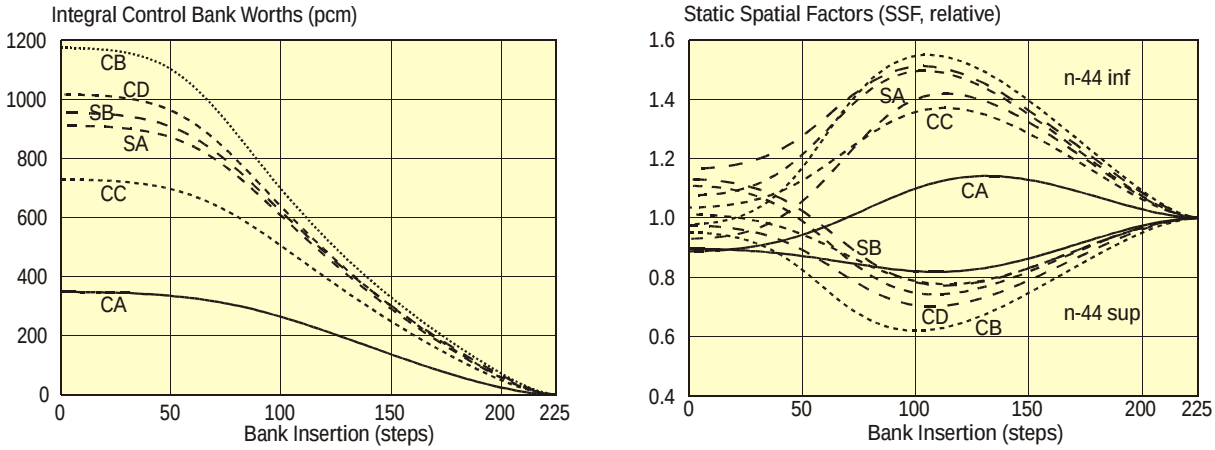

Figure 9. Integral control bank worth (left), in pcm and Static Spatial Factors (right) of excore chamber n44 versus bank insertion, in steps.

The banks with higher worth induce a larger shift of the neutron flux towards the core bottom, thus a larger difference of the excore currents (ΔI more negative). When the banks are fully inserted (0 steps at left), the SSF are different from unity due to the radial flux redistribution, so that banks located in the core center increase the neutron leakage and excore currents when inserted.

4.1.2. Transient Calculations of the Dynamical Rod Worth Measurement

The DRWM [19] is performed during the physical tests at beginning-of-life (BOC) of every cycle, after the first criticality and the measurement of the boron concentration with the all-rods-out (ARO) endpoint, below the Doppler nuclear heating level. Then, a slow boron dilution is done with a reactivity effect of about 60 pcm, inserting in advance the control bank CD, to achieve a stable critical state at 25% of the Doppler level, with the control bank inserted at about 200 steps.

In the simulation of the test, we start from this initial steady-state, at 0.025% of rated power with bank CD inserted at 200 steps, searching for the critical boron concentration. To achieve that initial steady-state independently of cycle, we start from the critical state at BOC-HZP-ARO and search for a control bank CD insertion that yields –60 pcm of reactivity and then we search for the critical boron.

Then, the control bank is withdrawn at the maximum allowed speed (74 steps/minute), bringing the core in about 25 seconds to +60 pcm supercritical with delayed neutrons, since this reactivity is only about 10% of the delayed neutron fraction at BOC (0.6 %). This excursion is slow and asymptotic (with fixed ARO condition) bringing the core to 75 % of the Doppler level in about 100 seconds. At that moment the quick insertion of the bank to measure is started, also at the maximum allowed speed of 74 steps per minute. After about 3 minutes the bank reaches its full insertion, which is kept only for about 15 seconds. Afterwards, the bank is withdrawn at the same speed, in 3 minutes, and the ARO state is kept, waiting for about 400 seconds to recover flux level of 75% of the Doppler, to initiate the same sequential test for other bank.

Figure 10 (left) shows the insertion, in steps, of each bank versus time given as input to the SIMTRAN code. Figures 10 (right) and 11 (left) show the evolution of the dynamical reactivity and of the average core power for the calculations of the DRWM tests of each control bank. SIMTRAN calculates the dynamical reactivity by inverse point kinetics from the evolution of the 3-D core average power

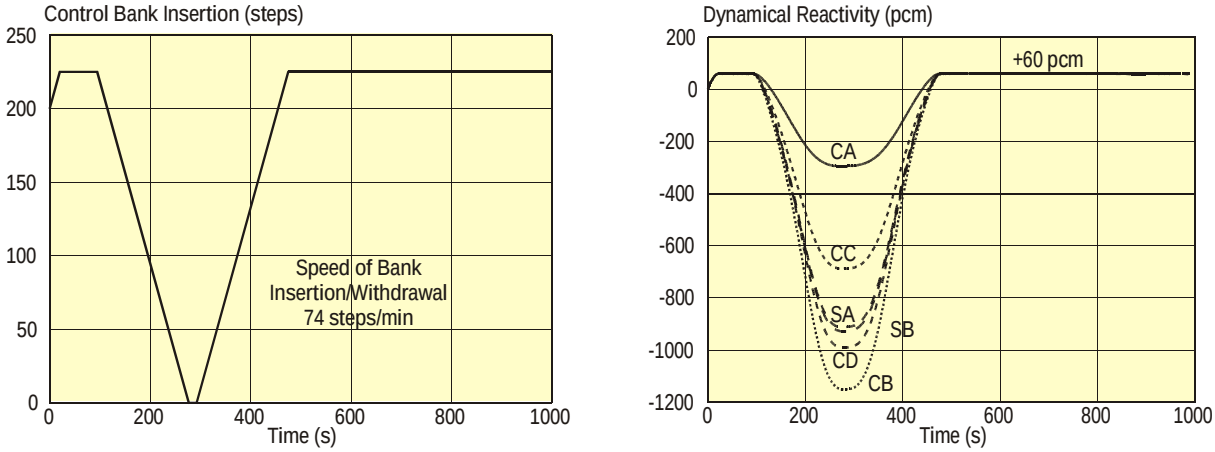

Figure 10. Control bank insertion (left) vs. time used and Dynamical reactivity (right) vs. time calculated by SIMTRAN in the transient for Dynamic Rod Worth Measurement for all control banks.

The measured currents at the excore detectors N-44 superior and inferior are shown in figure 11 (right), together with the currents calculated by SIMTRAN, normalized to the measured ones at the initial time. The agreement in the evolution of the currents is quite good, with a bit larger axial difference (ΔI) of the calculated currents, compared with the measured ones, at intermediate bank insertions.

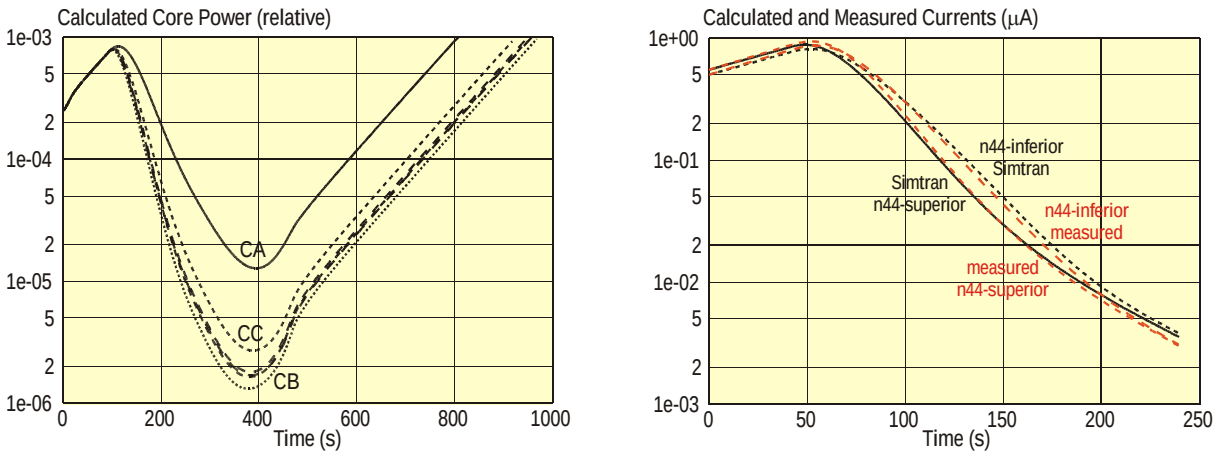

Figure 11. Calculated core power (left) for all control banks and calculated and measured currents at excore detector n44 (right) vs. time for control bank CB in the DRWM transient.

Figure 12 shows the time evolution of the exponential frequencies of the core power (left) and of the sources of the 6 delayed neutron precursors (right).

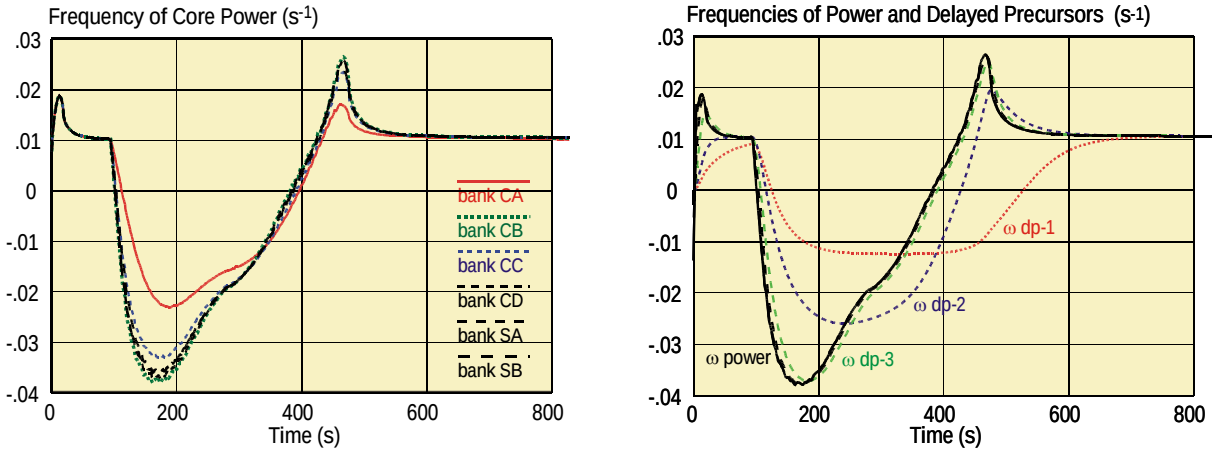

Figure 12. Calculated power frequencies (left) for all control banks and calculated power and delayed precursor groups frequencies (right) vs. time for control bank CB in the DRWM transient.

In this figure 12, the zero frequencies correspond to the maximum or minimum of the core power (left) or of the sources of the 6 delayed neutron precursors (right). The intervals with constant frequencies correspond to the asymptotic periods, after constant reactivity. The maximum or minimum frequencies are reached before the full withdrawal or insertion of each control bank, when the rate of increase or decrease of reactivity reaches also a maximum or minimum. The sources of the 6 delayed precursor groups follow the frequency of the core power with a delay related to the decay constants of each precursor (about 0.013, 0.032 and 0.12 s^{-1} for groups 1 to 3).

4.2 Analysis of the NEA/NSC benchmarks of control rod ejections and extractions

We have selected the two NEA Benchmarks for 3-D PWR transients [39], with rod ejections and bank withdrawals, and several model transients at conditions found in actual PWR operating cycles [24]. In the model transients just one variable is perturbed, while the others are kept constant, and the control rods are not tripped or moved by the protection or automatic control systems. The objective is to address the key issues in the neutronics thermal-hydraulics coupling, in both very fast and slower transients.

4.2.1. NEA Benchmark of PWR Rod Ejection Transients at HZP

This benchmark includes 3 cases of fast ejections, in 0.1 s, of control rods from several initial configurations at hot zero power (HZP), with several control banks totally or partially inserted. The benchmark specifications were published by *Finnemann et al.* in NEACRP-L-335 (1992) and the inter-comparison results of the codes in reference [39].

The 3 cases are prompt supercritical, the ejected rod worth reactivity ρ exceeds the delayed neutron fraction β, in factors given in dollars as:

- Case A1: 1 central rod ejected in 1/8 core, $\rho = 1.068$ \$
- Case B1: 4 peripheral rods ejected in 1/8 core, $\rho = 1.093$ \$
- Case C1: 1 peripheral rod ejected in full core, $\rho = 1.262$ \$

In the point-kinetics approximation for prompt supercritical transients, the time derivative of the total neutron power quickly becomes proportional to the power, resulting in an exponential evolution of constant frequency ω_p, given by:

$$\frac{dp(t)}{dt} \approx \frac{\rho-\beta}{\Lambda}\,p(t) \quad \longrightarrow \quad p(t) = p_0 \exp\left(\frac{\rho-\beta}{\Lambda}\,t\right) \quad \longrightarrow \quad \omega_p = \frac{\rho-\beta}{\Lambda} \tag{14}$$

where Λ is the mean neutron generation time. In other words, the dominant eigenfrequency ω_p is rapidly reached and is constant until fuel heating quenches the excursion by Doppler feedback. Large power redistributions are observed within a time of order Λ after the rod ejection and afterwards the power shape or distribution is constant, given by the flux eigenfunction of the eigenvalue ω_p.

When fuel heats, after a time constant given by the fuel heat capacity, the fuel to clad conductance and the clad to water heat transfer, the reactivity ρ and the frequency ω_p quickly decrease by the Doppler effect as a function

of the effective fuel temperature. They decay to zero rather slowly, with the larger half-life of the delayed neutron precursor group.

We have calculated these 3 cases at HZP, as well as the 3 other cases at HFP, with our more recent version of SIMTRAN [24]. The agreement with the reference results is quite good. In the critical initial steady-state Boron concentration our average and standard deviations are 0.0 ±0.6 ppm. The ejected rod worth deviations are -1 ±4 pcm. The deviations in fuel and water temperatures are below ±0.5 percent. The power peaks of the HFP cases are well predicted, within 0.3 percent, but the power peaks of the HZP cases are still underpredicted, about -13 ±8 percent, although the energy release and fuel temperature evolution are in good agreement.

Our results for the 3 cases at HZP are summarized in figure 13, including the reactivity, frequency, power and Doppler fuel temperatures. The dynamical reactivity is calculated by SIMTRAN at every time-step, as the reactivity that in the point kinetics equation would yield the same total power frequency (this is referred as "inverse point kinetics").

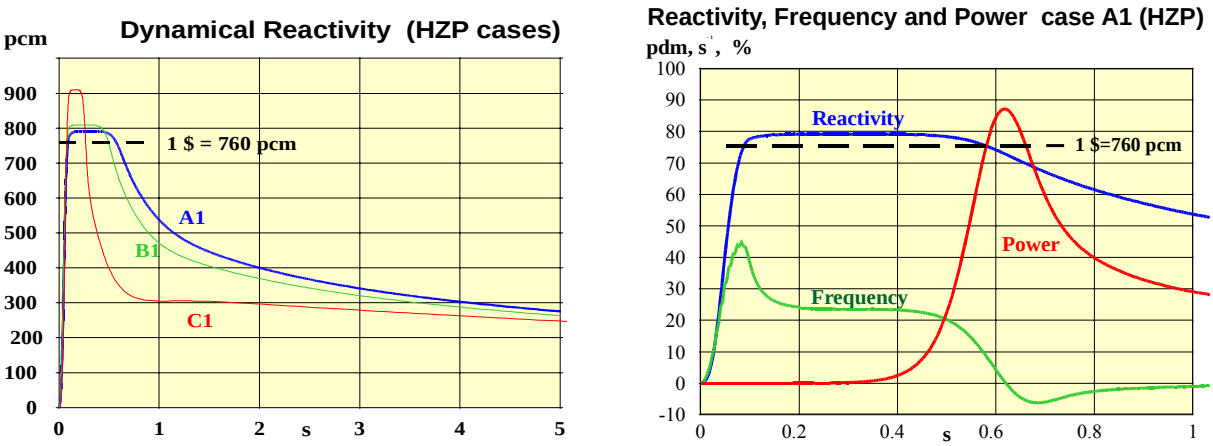

Figure 13. Reactivity, frequency and total power in rod ejection transients at HZP

The core average frequency ω_p, given by the logarithmic derivative of the total core power, shows a peak just before the end of the rod ejection (0.1 s), when the reactivity increase rate slows down, then goes down to the constant asymptotic eigenfrequency of the ejected rod HZP state.

The essential SIMTRAN results are compared in the next figure 14, together with the solution adopted as reference (PANTHER) and other codes. The differences in the total core power evolution are larger for case A1 (ρ just > β), because SIMTRAN calculates a bit lower ejected rod worth. Case C1 has larger reactivity and power peak, but less liberated energy, because the Doppler feedback actuates before, since the fuel heats with the energy (integral of power). The agreement in the fuel heating, and thus in the total energy liberated, is quite good.

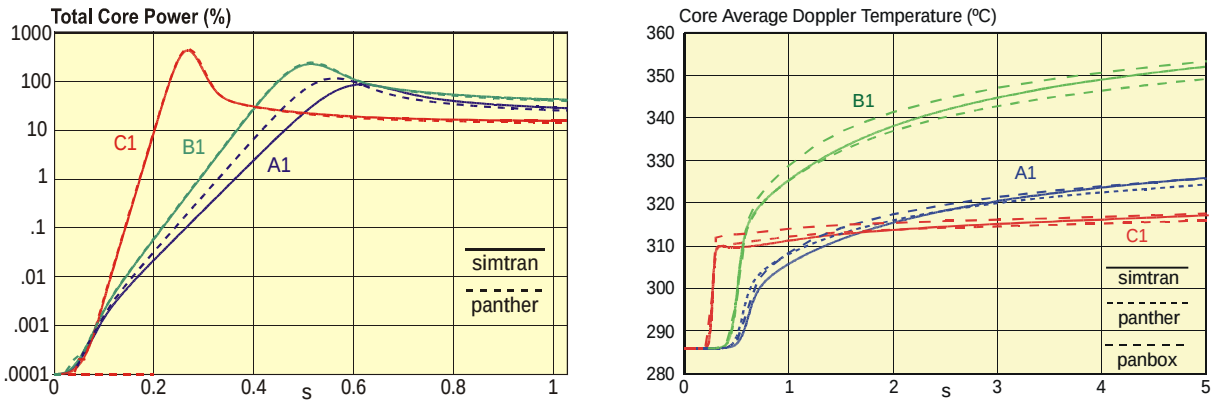

Figure 14. SIMTRAN results for NEA Benchmark of Rod Ejection Transients at HZP

4.2.2. NEA Benchmark of PWR Rod Ejection Transients at HFP

In these cases, with rod ejections similar to those at HZP, as shown in figure 15, the power increase is much lower because the ejected rod worth is much smaller, since the rod is initially less inserted, due to the insertion limits at power, and the fuel is initially very hot, so that the Doppler actuates inmediately. The agreement achieved in power is about 0.3 %. The agreement in fuel temperatures, and thus in the total energy liberated is quite good.

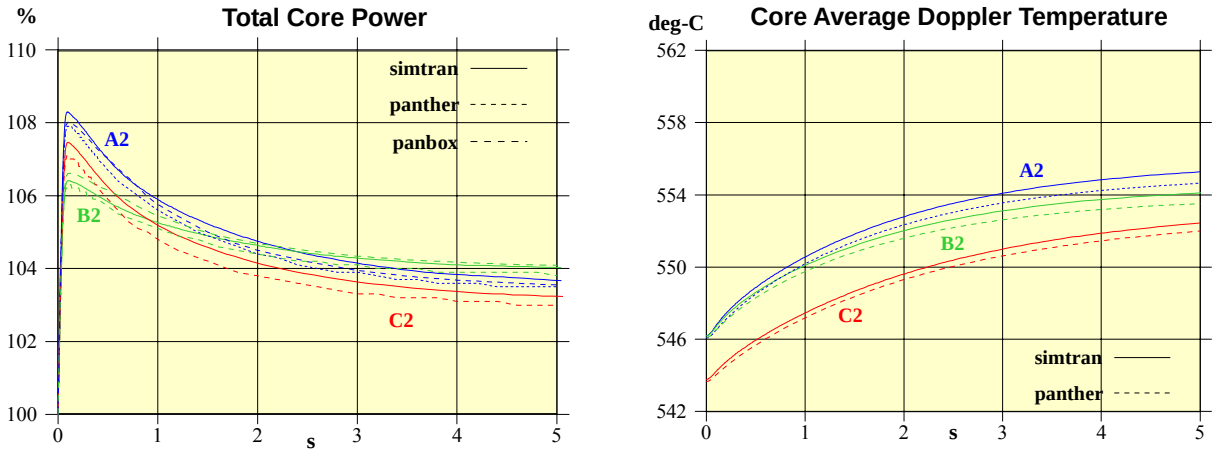

Figure 15. Total power and fuel temperature in rod ejection transients at HFP

4.2.3. NEA/NSC Benchmark of PWR Bank Withdrawal Transients at HZP

In this benchmark, 3 different control banks are withdrawn, at constant speed of 72 steps per minute, from 2 different initial control bank insertions, with critical Boron, at very low power (1.e-13 of nominal power). The core layout, 2-group cross-sections sets and thermal-hydraulics conditions are the same as in the previous NEA benchmark. At 0.6 seconds after reaching 35 percent of nominal power, all control rods are tripped down at constant speed, during 2.2 seconds for the full travelling length. The benchmark specifications were published by *Fraikin et al.* in NEA/NSC/DOC(93)9 (1993) and the inter-comparison of results from different codes in NEA/NSC/DOC(96)20 (1997):

- Case **A**: 1 central bank withdrawn out of 2 inserted banks.
- Case **B**: 2 peripheral banks withdrawn out of 4 inserted banks.
- Case **D**: 2 intermediate banks withdrawn out of 4 inserted banks.

The selected SIMTRAN results for the 3 cases are given in figure 16, reactivity and power, and figure 17, fuel average (Doppler) and maximum temperatures, together with the reference PANTHER results. In these transients the power excursion is limited, either by the Doppler feedback or by the programmed trip (in the low power range) at 35 % of power, with a 0.6 s delay. The critical variable is the specific energy or heat deposited in the fuel (in cal/g or J/Kg), that should by kept below the fuel fragmentation limit.

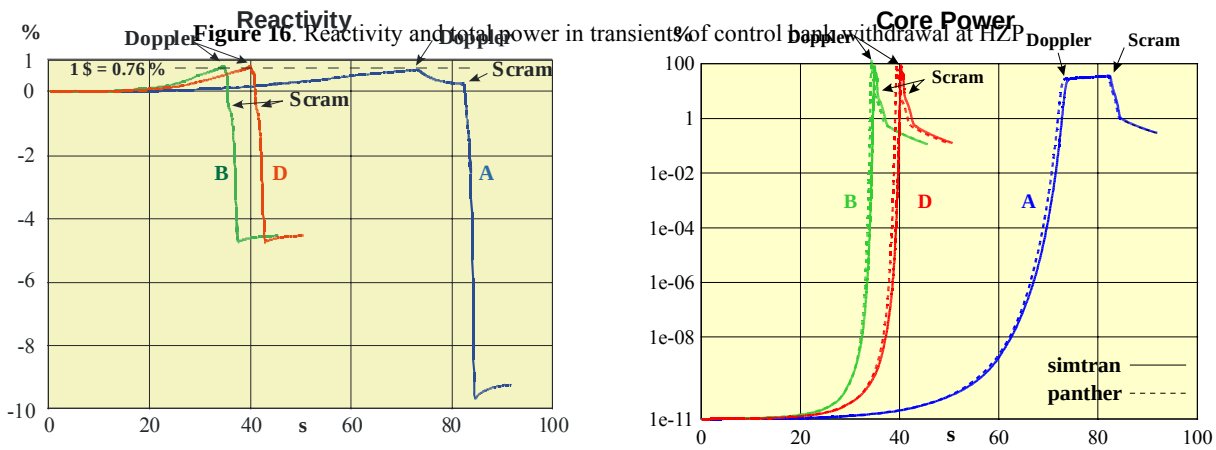

Figure 16. Reactivity and total power in transients of control bank withdrawal at HZP

Reactivity rise is slower in case A, with a single control bank withdrawal, that in cases B and D, with 2 banks withdrawal, so that in case A the power excursion is slower and is quenched by Doppler fuel heating just below 35 % power and control rod trip is delayed, but the rod trip is more antireactive since more control banks are initially out in this case. In cases B and D, since two banks are withdrawn, the excursions are much faster and yield a much higher power peak, limited by the trip activated at 35% power, with a delay of 0.6 s. The power redistribution (FQt) is also higher, but the energy yield and heating is much lower.

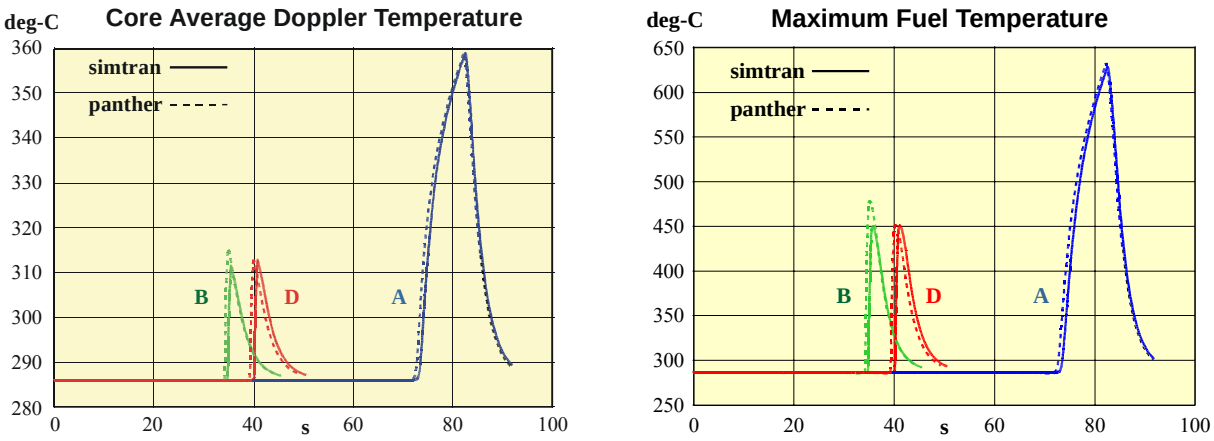

Figure 17. Average Doppler and maximum fuel temperatures in control bank withdrawals at HZP

4.3. Analysis of model prototype core transients in PWR with the SIMTRAN code

We analyze some prototype core transients with a single cause, by change in one single core input or control variable with the others kept constant and without scram (like in ATWS), but that show a significant redistribution of the neutron flux and power. All of them are calculated with our SIMTRAN code for an operating 3-loop Westinghouse PWR (Vandellós-II Cycle-9) [24].

4.3.1. Model Rod Ejection Transients at several powers and cycle burnups

We have done a systematic analysis of rod ejection transients at several initial power levels and core states along nominal cycle burnup. In these transients, the most reactive rod is ejected, in 0.1 seconds, from the rod insertion limit, that is a linear function of power level. The SIMTRAN results for the total core power evolution are collected in figure 18, at several initial powers and cycle burnups.

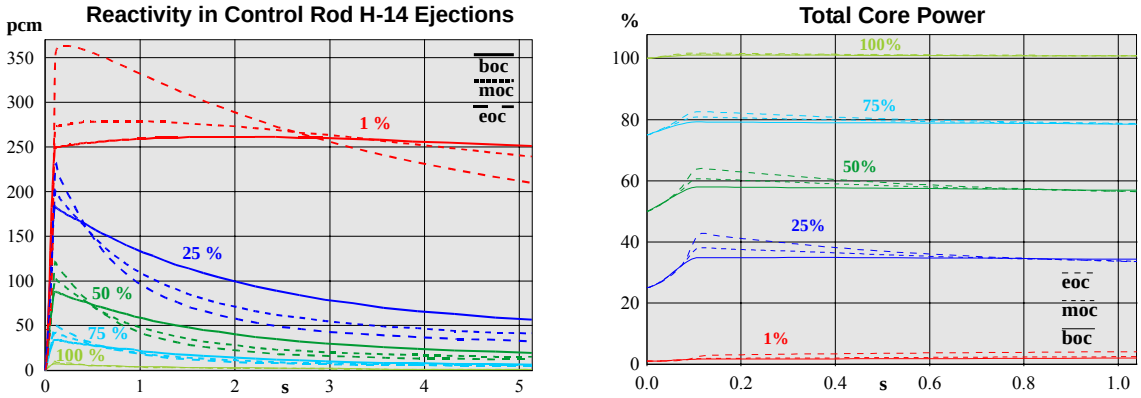

Figure 18. Reactivity and total power in transients of control rods ejected from their insertion limits at 100, 75, 50, 25 and 1 % power, at BOC, MOC and EOC.

The reactivity of the worst ejected rod increases with the cycle burnup, because then the power is shifted towards the core periphery, where the most reactive control rod (H-14) is located. The rod worth is larger at low powers, because the axial offset of power is the more positive and the rod is ejected from a deeper insertion. All

these excursions result in only moderate increases of the total power, showing the adequacy of the control rod insertion limits as a function of the power level. The higher power rise occurs at 25 % initial power and end-of-cycle (EOC), with a peak of ≈42 %. At 1 % initial power the power excursion is quite slow and limited, even with the higher rod ejection worth, due to that in this case it starts from full insertion.

4.3.2. Effect of Xenon and Axial Offset in Rod Ejection Transients at EOC-HZP

We have investigated the effect of Xenon buildup and decay, after shutdown from nominal equilibrium conditions at EOC, on the axial offset of incore power and, hence, on the worth of the worst ejected rod at HZP critical state with the control banks just in the insertion limit; and, finally, on the rod ejection transient. In figure 19, we include the effect of the Xenon peak on the axial offset of power and the worth of the worst ejected rod, as a function of the shutdown time in hours.

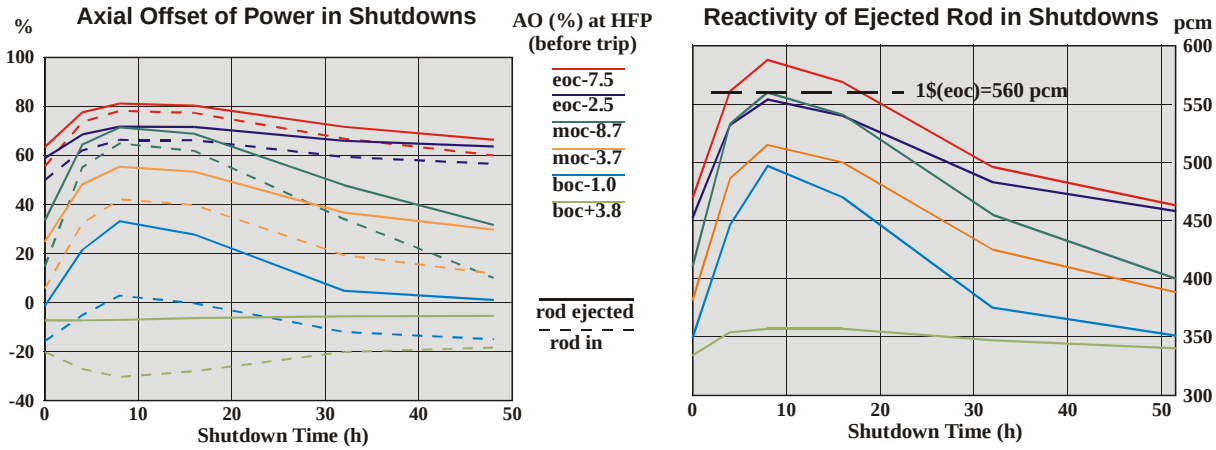

Figure 19. Axial offset of power and reactivity of the worst ejected rod at HZP after shutdowns

The Xenon peak causes a more positive axial offset of power, that is more positive with the cycle burnup and the power axial offset of the previous operation, and this increases the ejected rod worth from 470 pcm, at 0 h EOC, that is much below the prompt supercritical limit (given by the effective delayed neutron fraction, 560 pcm at EOC in this cycle and larger at BOC), to a value of 590 pcm at the Xenon peak, at 8 h EOC, that is over the prompt supercritical limit.

In these cases the Xenon was at the nominal equilibrium conditions at HFP, all rods out (ARO), when the power axial offset at EOC was -2.5 %. Since PWRs are allowed to operate at full power with the control bank partially inserted, but with the power axial offset within a band of ±5 % of the previous nominal value, so that the axial offset of the Xenon concentration can also be out of the nominal value. The worst condition, for increased ejected rod worth, is with the most negative axial offset of power and Xenon at HFP, as considered next. In figure 20, we compare the results, in reactivity and total power, of the ejections of the worst control rod (H-14) at HZP, at 0 and 8 hours of shutdown after trip from the worst axial offset at full power (at EOC, A.O.= -7.5 %). The worst case, at the Xenon peak at 8 hours of shutdown after trip, is just promt supercritical, but the power excursion terminates at 4.5 % of power and the final power, at 50 s of the transient, is similar in both cases.

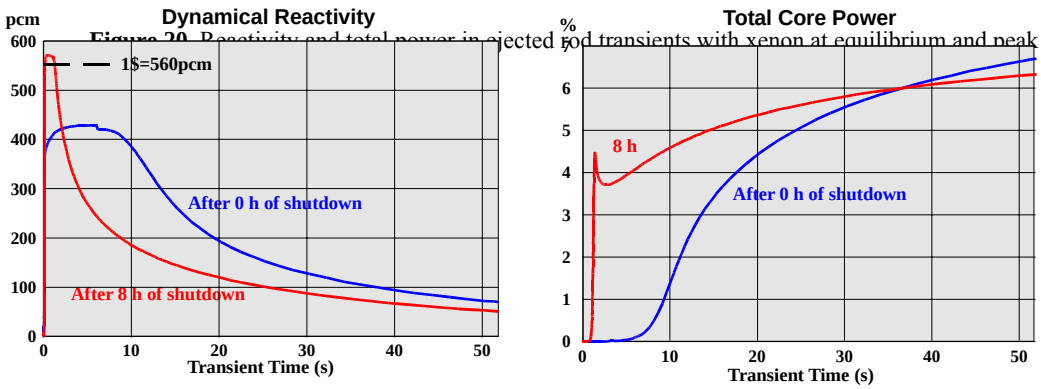

Figure 20. Reactivity and total power in ejected rod transients with xenon at equilibrium and peak

4.3.3. Model Control Bank Withdrawal Transients at EOC-HZP and Xenon peak

We have performed analysis of model transients with control bank withdrawals of maximum best-estimate worth, at EOC-HZP with the worst moderator temperature coefficient and the worst axial offset of power at the Xenon peak, 8 hours after shutdown from nominal equilibrium conditions, and the control banks D+C at the insertion limit at HZP.

Results of the evolution of dynamical reactivity and total core power are given in figure 21, for the withdrawal at 72 steps per minute of bank D alone and banks D+C together, with the initial overlap. In the bank D withdrawal, the core power stabilizes just below 35 %, the protection setpoint at low power. In the withdrawal of banks D+C, that is not an anticipated transient, the core power stabilizes just below 60 %, without any power or temperature peak. Remember that these are model transients, with constant flow and temperature at core inlet and without scram.

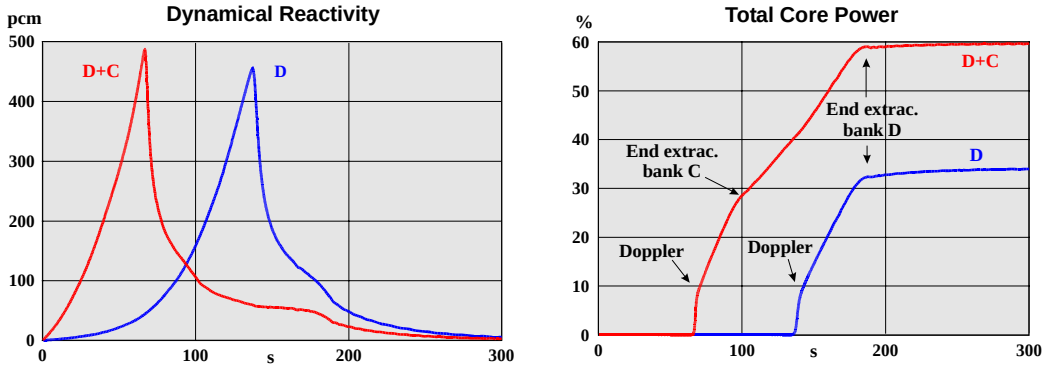

Figure 21. SIMTRAN results for reactivity and total power in bank withdrawal transients at EOC-HZP-critical, after 8 hours shutdown from HFP-Eq.Xe, with maximum effect of Xenon and axial offset.

In the withdrawal of a single control bank (case D), the reactivity insertion is slower and the total core power stabilizes, at the end of the withdrawal, just below 35 % power (the *setpoint* for trip). In the withdrawal of two control banks (case D+C), the reactivity insertion is master and the total core power increases to 60 %, after the end of the withdrawal, without peaks in power or temperature.

References

1. G.I. Bell, S. Glasstone, "*Nuclear Reactor Theory*", Van Nostrand Reinhold, New York (1970).
2. A.F. Henry, "*Nuclear Reactor Analysis*", The MIT Press, Boston (1975).
3. J.J. Duderstadt, L.J. Hamilton, "*Nuclear Reactor Analysis*", John Wiley & Sons, New York (1976).
4. E.E. Lewis, "*Nuclear Power Reactor and Safety*", John Wiley & Sons, New York (1977).
5. K.O. Ott, D.A. Meneley, "*Introductory Nuclear Reactor Dynamics*", ANS, Chicago (1985).
6. J.M. Aragonés, J.M. Martínez-Val, M.R. Corella, "*Core State Models for Fuel Management of Equilibrium and Transition Cycles in Pressurized Water Reactors*", Nuclear Technology **34-3**, 398-411 (1977).
7. G. Velarde, C. Ahnert, J.M. Aragonés, "*Analysis of the Eigenvalue Equations in k, λ, γ and α Applied to Fast and Thermal Neutron Systems*", Nucl. Sci. Eng. **66-3**, 284-294 (1978).
8. J.M. Aragonés, "*Detailed Calculations in Energy and Space of Effective Neutron Resonance Cross Sections*", Nucl. Sci. Eng. **68**, 281-298 (1978).
9. J.M. Aragonés, C. Ahnert, J. Gómez Santamaría, I. Rodríguez Olavaria, "*Development and Validation of Core Physics Methods for In-Core Fuel Management of PWRS*", in Reactor Physics and Core Thermal Hydraulics, NUREG/CP-0034, Vol. I, 315, Kiamesha Lake (1982).
10. C. Ahnert, J.M. Aragonés, "*A Coupled Fine Coarse-Mesh Few-Group Diffusion Method*", Trans. Am. Nucl. Soc., **47**, 414 (1984).
11. C. Ahnert, J.M. Aragonés, "*Finite Difference Formulation for Coarse-Mesh Few-Group Diffusion Calculations*", Trans. Am. Nucl. Soc., **50**, 281 (1985).
12. C. Ahnert, J.M. Aragonés, "*Fuel Management and Core Design Code Systems for Pressurized Water Reactors*", Nucl. Technology, **69**, 350-367 (1985).
13. J.M. Aragonés, C. Ahnert, "*Linear-Discontinuous Finite-Difference Formulation for Synthetic Coarse-Mesh Few-Group Diffusion Calculations*", Nucl. Sci. Eng. **94**, 309-322 (1986).
14. C. Ahnert, J.M. Aragonés et al., "*Validation of the Pressurized Water Reactor Core Analysis System SEANAP*", Nucl. Sci. and Eng., **100**, 305 (1988).
15. A. Crespo, J.M. Aragonés, C. Ahnert, "*Pin Power and Burnup Calculation by the SEANAP PWR Core Analysis System*", Proc. Int. Reactor Physics Conf., Vol. II, 65, ANS, Jackson Hole (1988).
16. J.M. Aragonés, C. Ahnert, "*Reactivity Effects of Fission Product Decay in PWR's*", Trans. Am. Nucl. Soc., **57**, 311 (1988).
17. J.M. Aragonés, C. Ahnert, A. Crespo, J.R. León, "*Isotopic Depletion of Soluble Boron in a PWR*", Trans. Am. Nucl. Soc., **57**, 314 (1988).
18. J.M. Martínez-Val, J.M. Aragonés, E. Mínguez, J.M. Perlado, G. Velarde, "*An Analysis of the Physical Causes of the Chernobyl Accident"*, Nuclear Technology **90**, 371-388 (1990).
19. F. Merino, C. Ahnert, J.M. Aragonés, *"Development and Validation of the 3-D PWR Core Dynamics SIMTRAN Code"*, in Mathematical Methods and Supercomputing in Nuclear Applications, H. Kusters (Ed.), Vol. 1, 646-657, ANS-KfK, Karlsruhe, (1993).
20. J.M. Aragonés, C. Ahnert, "*Computational Methods and Implementation of the 3-D PWR Core Dynamics SIMTRAN Code for Online Surveillance and Prediction*", in Mathematics and Computation, Reactor Physics and Environmental Analysis, L. Briggs (Ed.), Vol. 1, 237, American Nuclear Soc., Portland (1995).
21. J.M. Aragonés, C. Ahnert, O. Cabellos, "*Methods and Performance of the 3-D PWR Core Dynamics SIMTRAN Online Code*", Nucl. Sci. Eng. **124(1)**, 111-124 (1996).
22. O. Cabellos, C. Ahnert, J.M. Aragonés, "*Generalized Effects in Two-Group Cross Sections and Discontinuity Factors for PWR's*", Proceedings of the International Conference on the Physics of Reactors (PHYSOR 96), Mito, Ibaraki (Japón), Vol. 1, B-82-91 (1996).

23. J.M. Aragonés, C. Ahnert, D. Cano, N. García-Herranz, "*Planing of Operational Maneuvers with the 3-D PWR Core Dynamics SIMTRAN Online code*", Proceedings of the International Conference on the Physics of Reactors (PHYSOR 96), Mito, Ibaraki (Japón), Vol. 4, K-9-17 (1996).

24. J.M. Aragonés, C. Ahnert, V. Aragonés-Ahnert, *"Coupled 3-D Neutronic-Thermalhydraulic Analysis of Transients in PWR Cores"*, in Mathematical Methods and Supercomputing for Nuclear Applications, F. Brown (Ed.), Vol. 2, 1380-1390, American Nuclear Soc., Saratoga (1997).

25. C. Ahnert, J.M. Aragonés, O. Cabellos, N. García-Herránz, "*Continuous Validation and Development for Extended Applications of the SEANAP Integrated 3-D PWR Core Analysis System*", in Mathematics and Computation, Reactor Physics and Environmental Analysis in Nuclear Applications, J.M. Aragonés (Ed.), Vol. 1, 710-719, Senda Ed., Madrid (1999).

26. N. García-Herranz, J.M. Aragonés, O. Cabellos, C. Ahnert, "*Dependence of the Nodal Homogenized Two-Group Cross Sections on Intranodal Flux-Spectrum, Burnup and History*", in Mathematics and Computation, Reactor Physics and Environmental Analysis in Nuclear Applications, J.M. Aragonés (Ed.), Vol. 1, 127-138, Senda Ed., Madrid (1999).

27. O. Cabellos, J.M. Aragonés, C. Ahnert, "*Generalized Effects in Two Group Cross Sections and Discontinuity Factors in the DELFOS Code for PWR Cores*", in Mathematics and Computation, Reactor Physics and Environmental Analysis in Nuclear Applications, J.M. Aragonés (Ed.), Vol. 1, 700-709, Senda Ed., Madrid, (1999).

28. J.M. Aragonés, "*Coupled 3-D Neutronic and Thermal-Hydraulic Transient Calculations for Deterministic Safety Analysis*", Frederic-Joliot–Otto-Hahn Summer School on Reactor Physics, CEA, Cadarache (2000).

29. J.M. Aragonés, C. Ahnert, O. Cabellos, N. García-Herranz, V. Aragonés-Ahnert, "*Methods and Results for the MSLB NEA Benchmark using SIMTRAN and RELAP-5*", Trans. Am. Nuc. Soc. **84**, 23, Milwaukee (2001).

30. N. García-Herranz, O. Cabellos, J.M. Aragonés, C. Ahnert, "*Performance of the Analytic Coarse Mesh Finite Difference Method with Heterogeneous Nodes*", Physor-2002, International Reactor Physics Conference, Seoul (2002).

31. N. García-Herranz, O. Cabellos, J.M. Aragonés, C. Ahnert, "*Analytic Coarse Mesh Finite Difference Method Generalized for Heterogeneous Multidimensional Two-Group Diffusion Calculations*", Nucl. Sci. Eng. **144**, 23-35 (2003).

32. J.M. Aragonés, C. Ahnert, O. Cabellos, N. García-Herranz, V. Aragonés-Ahnert, "*Methods and Results for the MSLB NEA Benchmark using SIMTRAN and RELAP-5*", Nuclear Technology **146**, 29-40 (2004).

33. M.R. Wagner, K. Koebke, H.J. Winter, "*A Non-Linear Extension of the Nodal Expansion Method*", in Mathematical Methods for the Solution of Nuclear Engineering Problems, Vol. 2, 43, Munich (1981).

34. K. Koebke, "*Advances in Homogenization and Dehomogenization*", in Mathematical Methods for the Solution of Nuclear Engineering Problems, Vol. 2, 59, Munich (1981).

35. K.S. Smith, "*Assembly Homogenization Techniques for Light Water Reactor Analysis",* Prog. Nucl. Energy, **17**, 303 (1986).

36. Y.A. Chao, "*A Theoretical Analysis of the Coarse Mesh Finite Difference Representation in Advanced Nodal Methods*", in Mathematics and Computation, Reactor Physics and Environmental Analysis in Nuclear Applications, J.M. Aragonés (Ed.), Vol. 1, 117-126, Senda Ed., Madrid, (1999).

37. Y.A. Chao, "*Coarse Mesh Finite Difference Methods and Applications*", in Advances in Reactor Physics and Mathematics and Computation into the Next Millennium (PHYSOR 2000), Vol. 2, 9404, American Nuclear Soc., Pittsburgh, (2000).

38. Y. A. Chao, D. M. Chapman, D. J. Hill, L. R. Grobmyer, "*Dynamic Rod Worth Measurement*", Nuclear Technology, **132**, 403 (Dic. 2000).

39. H. Finnemann, H. Bauer, A. Galati, R. Martinelli, "Results of LWR Core Transient Benchmarks", *Nucl. Energ. Agency, OECD Paris*, NEA/NSC/DOC(93)25 (1993).

40. J.M. Aragonés, C. Ahnert, N. García-Herranz, "*The Analytic Coarse-Mesh Finite Difference Method for Multigroup and Multidimensional Diffusion Calculations*", Nucl. Sci. Eng. **157**, 1-15 (2007).